CHAPTER IV

LIGHT SCATTERING SIMULATIONS OF INTERSTELLAR GRAPHITE AND FAYALITE DUST ANALOGUES

4.1 Introduction

Graphite and fayalite are two major components of interstellar dust. It is evident that the cosmic and interstellar dust particles are formed with diverse structures and most of them are found to be complex mixtures of graphite and metal silicates [1-5]. Also these particles are revealed to be mostly in amorphous form [6]. All the elements that supposed to consist the dust systems are thoroughly studied by research groups with various compositions and size distributions. But to validate the computational models experimental evidences are needed. Simulations with analogue samples of graphite and silicate is a significant way to develop computational models of interstellar dust.

This chapter provides a description of the computational and experimental light scattering studies of interstellar dust analogue samples of graphite and fayalite.

4.2 Light scattering studies of graphite

A realistic model is employed to calculate the light scattering intensity profiles and degree of linear polarization of graphite dust with DDSCAT [7, 8]. The dust particles used in the experimental study ranges in size from 0.5 to 5.0 μm. A number of target geometries were generated as representative of the laboratory sample considering various physical properties like shape irregularities, surface roughness and aggregation states. Further to demonstrate the efficiency of the theoretical model a comparative study of computational phase functions (F_{11}) and degree of linear polarizations ($-\frac{F_{12}}{F_{11}}$) are performed with the experimentally measured values.

Using BLENDER3D a few target geometries are created [9]. After that the generated targets are converted into dipole arrays using DDSCATConvert online tool [10]. The dipole positions are then provided to DDSCAT 7.3.0 for carrying out the computation (Detailed target generation process is provided in Chapter 3: Section 3.1 Computational techniques).

In the first step of the simulation process two irregular geometries or model shapes (Model shape1 and shape2) are developed based on scanning electron microscopy (SEM) images (shown in Figure 4.7) of the graphite dust analogue samples (acquired from Sigma-Aldrich). To find out a best fit to the experimentally acquired results three different target

geometries are generated for each of the two model shapes. For realization of the model shapes into the target geometries, three approaches were applied. Moreover, each of the target geometries (total 6 in this case, 3 for model shape1 and 3 for model shape2) were represented using two sets of dipole arrays, one with 25465 dipoles and the other with 34681 dipoles. This has been done in order to study the effects of dipole number on scattering profiles of target and take into account porosity in the sample to some extent. The dipole numbers are selected in such way that the lattice dispersion relation, $|m|kd \leq 1$ is satisfied for majority of the particle sizes. This condition is critical for accurate calculation of scattering parameters as well as the efficiencies.

The target generation approaches are explained as below,

a) Target1: The target particle is generated as a single irregular geometric shape having smooth surface with number of dipoles fixed at 25465 and 34681 to populate the entire volume. (Figure 4.1 for model shape1 and Figure 4.4 for model shape2).
b) Target2: The target particle is generated as a single irregular geometric shape with slightly deformed surfaces to account for surface roughness and minute morphological details with same sets of dipoles (Figure 4.2 for model shape1 and Figure 4.5 for model shape2).
c) Target3: The target particle is generated in the form of a synthetic aggregate composed of N smaller spherical monomers of radius r_n with the same effective volume as that of the single target particle with effective radius r (Figure 4.3 for model shape1 and Figure 4.6 for model shape2).

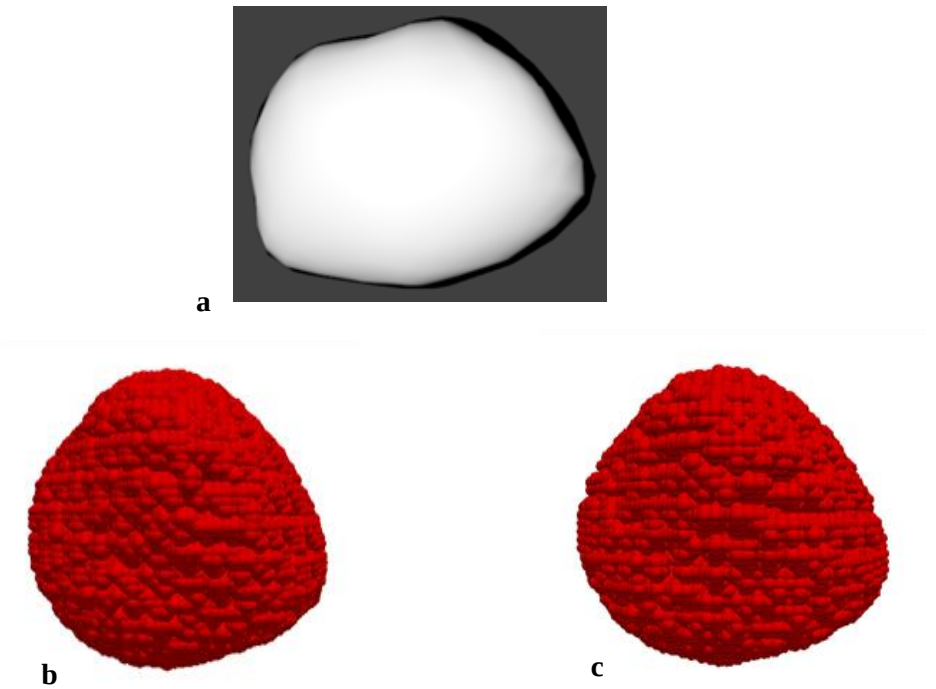

Figure 4.1 Target1 generated for the model shape1 (a) target modelled as a single irregular particle, (b) Dipole representation in 3D rendered form with 25,465 and (c) 34,681 dipoles respectively.

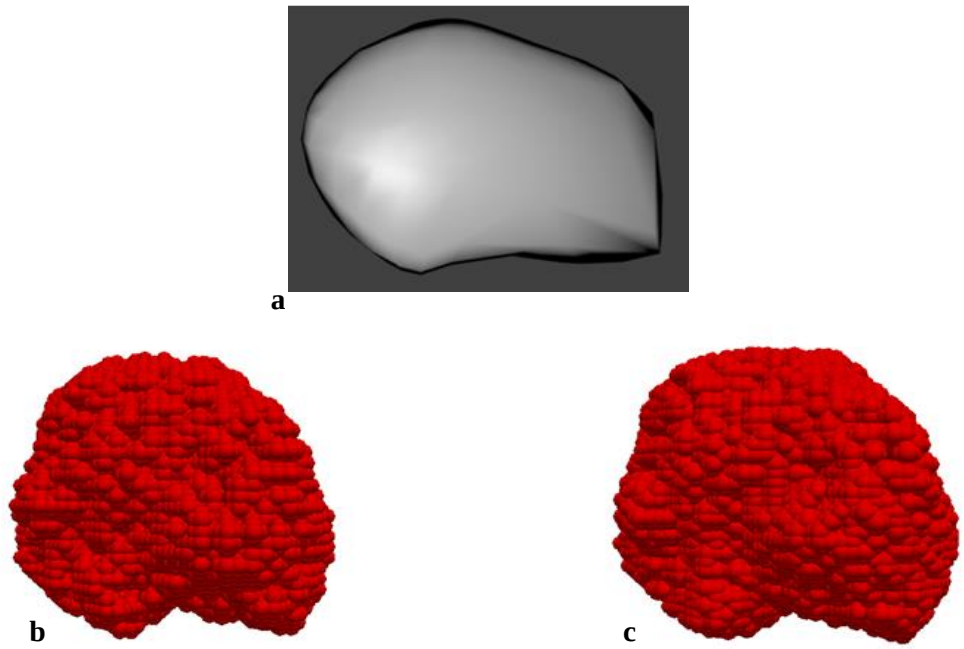

Figure 4.2 Target2 generated for the model shape1 (a) target modelled as a single irregular particle with added deformations to account for surface roughness (b) Dipole representation in 3D rendered form with 25,465 and (c) 34,681 dipoles respectively.

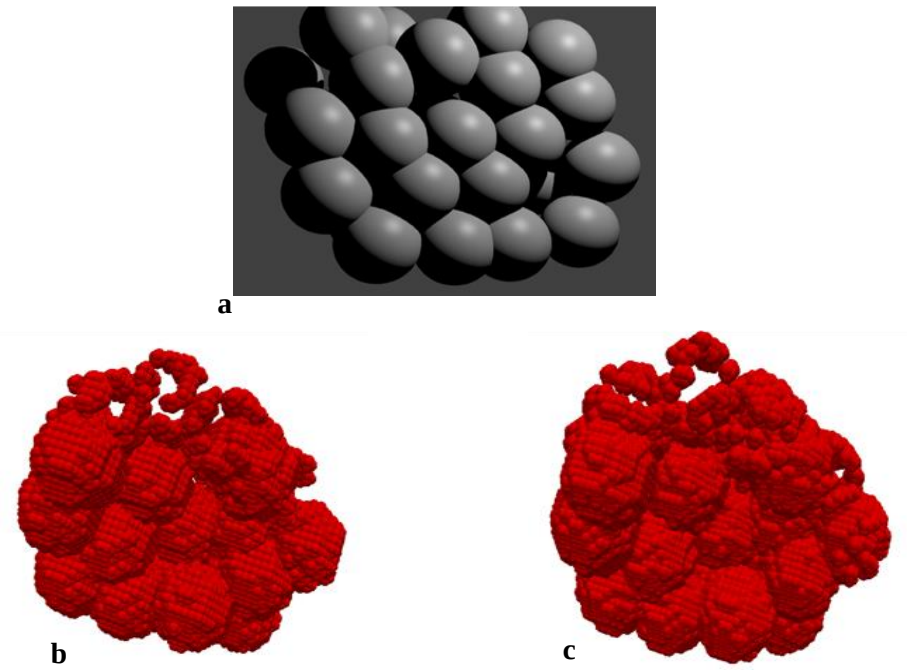

Figure 4.3 Target3 generated for the model shape1 (a) target modelled as aggregates of small spherical monomers (b) Dipole representation in 3D rendered form with 25,465 and (c) 34,681 dipoles respectively.

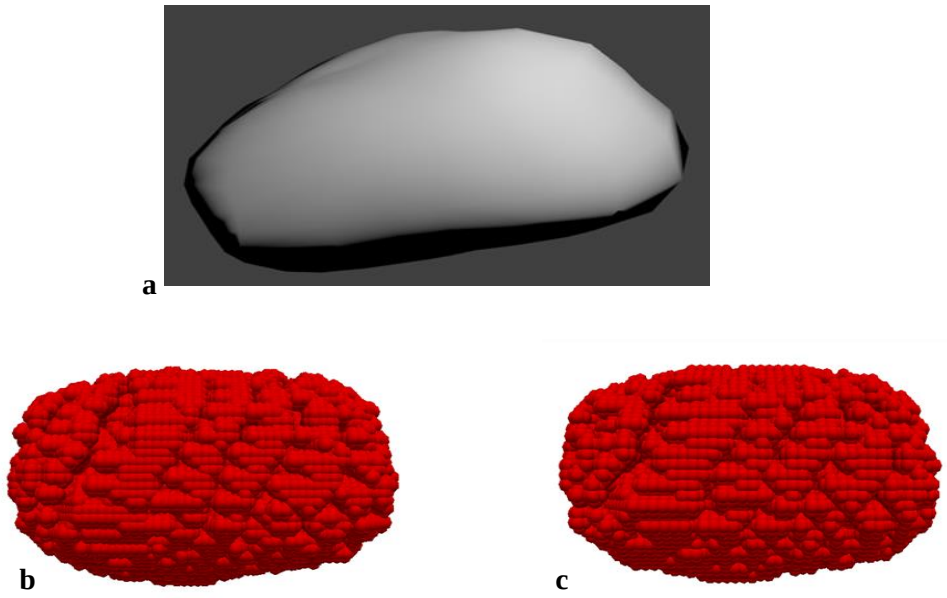

Figure 4.4 Target1 generated for the model shape2 (a) target modelled as a single irregular particle, (b) Dipole representation in 3D rendered form with 25,465 and (c) 34,681 dipoles respectively.

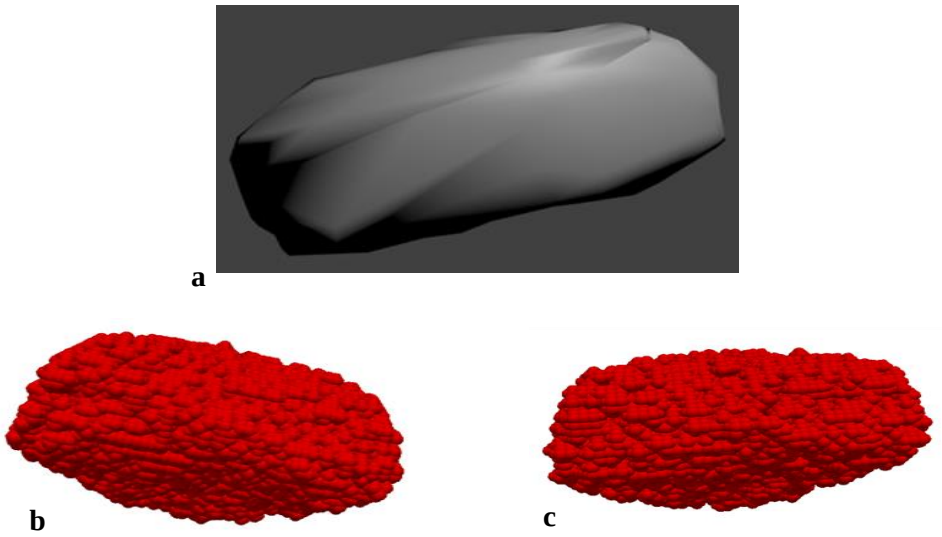

Figure 4.5 Target2 generated for the model shape2 (a) target modelled as a single irregular particle with added deformations to account for surface roughness (b) Dipole representation in 3D rendered form with 25,465 and (c) 34,681 dipoles respectively.

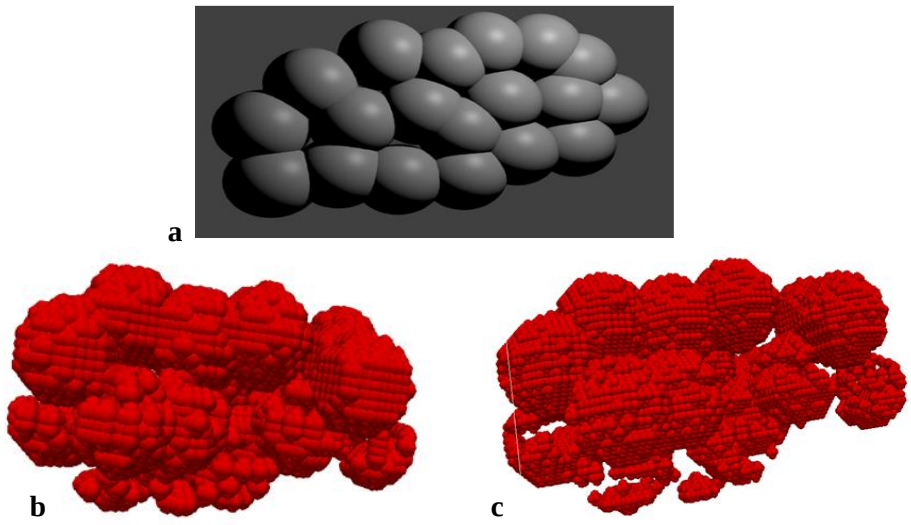

Figure 4.6 Target3 generated for the model shape2 (a) target modelled as aggregates of small spherical monomers (b) Dipole representation in 3D rendered form with 25,465 and (c) 34,681 dipoles respectively.

To generate the geometry target3 as an aggregate of spherical monomers the following equation is used to compute the effective radii [11].

$$r = N^{1/3} r_n \qquad \textbf{4.1}$$

where r is the effective radii of the volume equivalent sphere and r_n is the radius of each of the comprising spherical monomers.

4.2.1 Physical properties of the graphite particles

Selection of graphite as a scattering sample is justified since a number of astrophysical studies (e.g. interstellar extinction curves) revealed that carbonaceous particles are one of the major constituents of interstellar and cosmic dust clouds [12, 13]. A reasonable number of studies also suggest that the most important carbonaceous dust particles are highly irregular graphite, which could explain absorption and extinction features observed in the infrared region. Some studies also estimated the size distribution of graphite particles to be specifically in the range of a few 0.003 μm to 1 μm or more [14, 15].

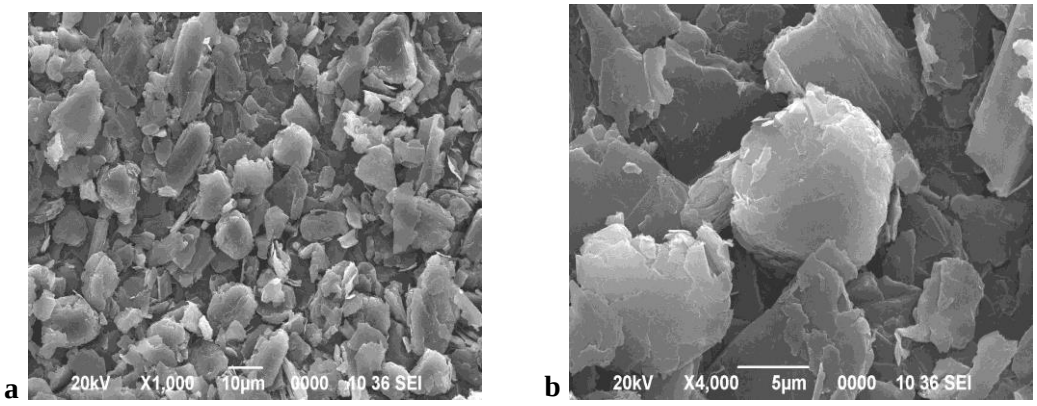

Figure 4.7 Scanning electron micrography (SEM) images of graphite particles.

The graphite samples used in the laboratory experiments are highly irregular as shown in SEM images (Figure 4.7 (a) and 4.7 (b)).For data reduction purpose the effective radii of the graphite particles are measured using scanning electron microscopy (SEM) images the most appropriate size distribution (in this case lognormal) is employed fit the samples. The particles are found to be distributed in sizes mainly within a range of 0.5 to 5 μm. A used

lognormal size distribution function is used to represent the particles with modal radius of 1.0 μm and standard deviation of 1.5. In order to the compute the scattering properties of shape and size dispersed ensembles DDSCAT7.3.0 along with the MATLAB© post processing tool was used.

This was performed by taking the output files generated by DDSCAT 7.3.0 for each of the shape and size considered as an input to the MATLAB© tool averaging with the size distribution function.

The lognormal size distribution is given by the equation [16],

$$n(r) = \frac{N}{\sqrt{2\pi}\ln\sigma_g}\exp\left[-\frac{(\ln r - \ln r_g)^2}{2(\ln\sigma_g)}\right] \qquad \textbf{4.2}$$

where r is the radius of the particle, $n(r)$ is the number of particles with radius r, σ_g is the standard deviation of the size distribution, r_g is the modal radius, N is the number concentration at modal radius. Table 4.1 provides size distribution of graphite.

Table 4.1 Particl**e** size distribution of graphite

Size Distribution	**Lognormal (Gaussian)**
Minimum particle radius	0.5 μm
Maximum particle radius	5.0 μm
Modal radius (r_g)	1.0 μm
Standard deviation (σ_g)	1.5

For carrying out calculation of the scattering matrices, the values of refractive indices were considered to be 2.73+1.560i and 2.80+1.628i respectively for the incident wavelengths 543.5 nm and 632.8 nm (Table 4.2).

Table 4.2 Refractive index of graphite

Wavelength	Refractive Index (real) n	Refractive Index (imaginary) k
543.5 nm	2.73	1.560
632.8 nm	2.80	1.628

4.2.2 Results and discussions

In this work, a comparative analysis of the experimentally measured and computational values of the scattering matrix element $F_{11}(\theta)$ and degree of linear polarization, $-F_{12}(\theta)/F_{11}(\theta)$ of interstellar graphite dust analogues are done. For this purpose, a laser based laboratory light scattering setup [17, 18] was used (Discussed in Chapter 3: 3.2.2. The experimental setup for optical characterization).

The computed and experimental values of $F_{11}(\theta)$ and $-F_{12}(\theta)/F_{11}(\theta)$ for each of the model shapes are plotted for 543.5 nm (Figure 4.8 for phase function and Figure 4.12 for polarization) and 632.8 nm (Figure 4.9 and Figure 4.10 for phase function and Figure 4.13 and Figure 4.14 for polarization) incident wavelengths and then for the combination of shapes for 543.5 nm and 632.8 nm incident wavelengths in Figure 4.11 (a) and 4.11 (b) for phase function and Figure 4.15 (a) and 4.15 (b) for polarization respectively.

The comparative analyses is performed in order to arrive at some suitable conclusion regarding the accuracy and efficiency of the size and shape averaged model of dust particles. For the comparison purpose, the following steps were followed:

1. In the first step the computational values of $F_{11}(\theta)$and $-F_{12}(\theta)/F_{11}(\theta)$were calculated for all the three generated targets of model shape1 with lognormal size distribution at 543.5 nm incident wavelengths.
2. In the next step the computational values of all the three target geometries generated for the model shape1 are plotted along with the experimental results for a comparative study.

3. Then the target geometry is selected for which the best fit (hereafter called as best target1) to experimental measurements are obtained. The best target was selected using root mean square error analysis and successive comparison.
4. Steps 1 to 3 were repeated in case of model shape2 to find the best fit (hereafter called as best target2) with the measurements.
5. In the next stage the effects of shape dispersions on theoretical simulation are studied by combining the results of both the shapes (best target1 and best target2) which most likely supposed to compose majority of the particles in our sample, for a more accurate and realistic modeling.
6. Steps 1 to 5 were repeated for comparison at the second incident wavelength of 632.8nm.
7. Moreover for 543.5nm wavelength the number of dipoles used are 34,681 but for the 632.8 nm wavelength the number of dipoles used are varied once for 25,465 and 34,681. The reason for this can be explained as: There is flexibility regarding the use of dipoles for wavelengths relatively more comparable to the particle sizes. As mentioned earlier two dipole sets are generated for the study. But for the smaller wavelength we always need to use the maximum dipole set to keep the values of $|m|kd$ closer to 1. This addition could provide a way to test the accuracy of our models for different number of dipoles.
8. The final computational values are obtained as Shape dispersions = Best target1 (from model shape1) + Best target2 (from model shape2).

The target particle orientation is DDA is defined by using three angles in the target frame namely β, ϕ and θ. The orientational averaging is achieved by running the β and ϕ from 0^0 to 360^0 and θ from 0^0 to 180^0. In this computation the number of directions considered for averaging are 48 [7].

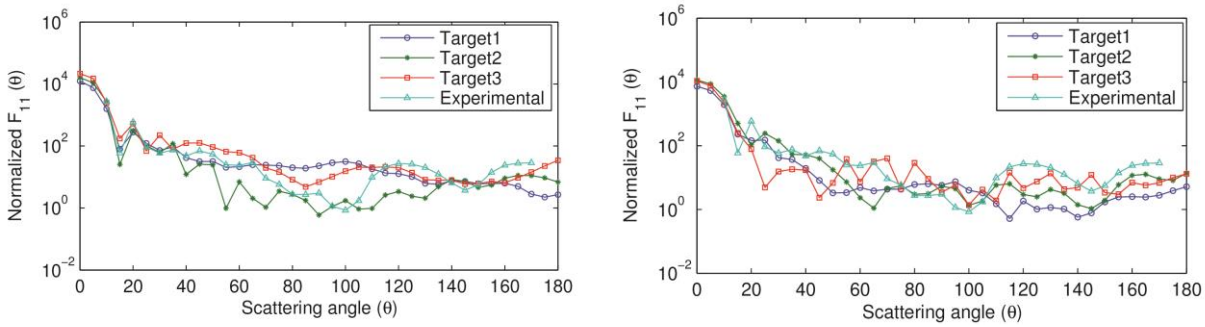

Figure 4.8 (a) Phase function for model shape1 at 543.5 nm incident wavelength with curves represented by symbols given in the legends indicating computed values of phase function for 3 targets and experimental values. (b) Phase function for model shape2 at 543.5 nm incident wavelength with curves represented by symbols given in the legends indicating computed values of phase function for 3 targets and experimental values.

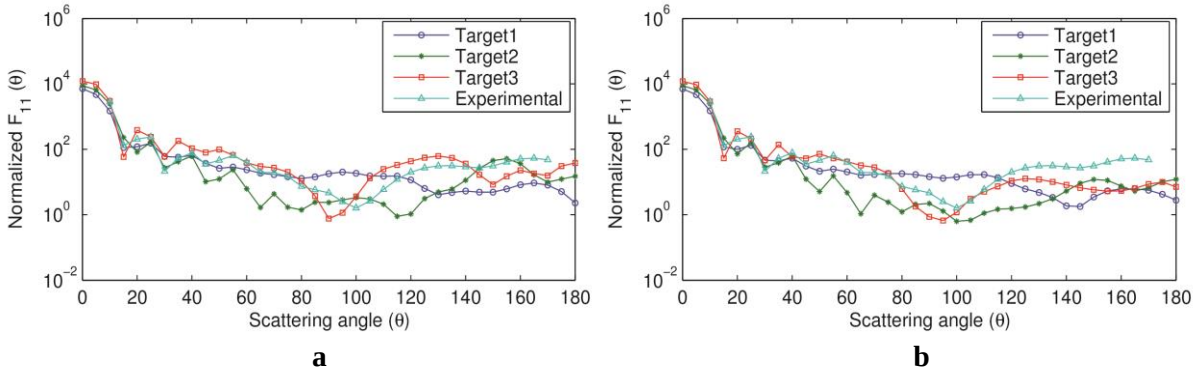

Figure 4.9 (a) Phase function for model shape1 at 632.8 nm incident wavelength (25,465 dipoles) with curves represented by symbols given in the legends indicating measured values of phase function for 3 targets and experimental values. (b) Phase function for model shape1 at 632.8 nm incident wavelength (34,681 dipoles) with curves represented by symbols given in the legends indicating measured values of phase function for 3 targets and experimental values.

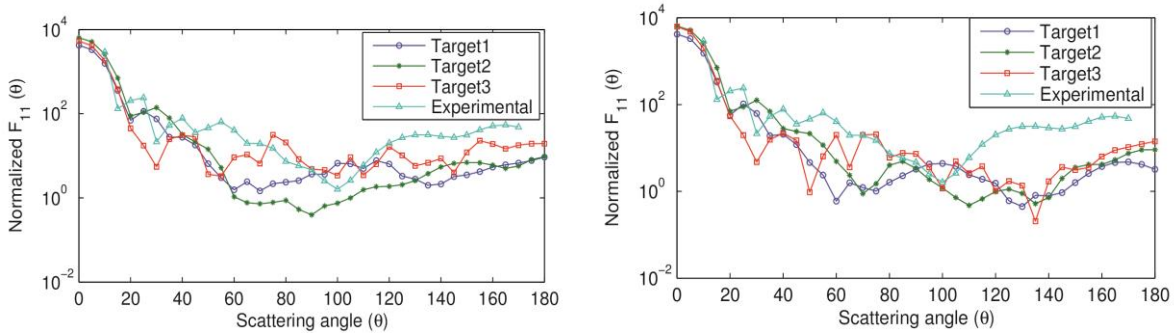

Figure 4.10 (a) Phase function for model shape2 at 632.8 nm incident wavelength (25,465 dipoles) with curves represented by symbols given in the legends indicating measured values of phase function for 3 targets and experimental values. (b) Phase function for model shape2 at 632.8 nm incident wavelength (34,681 dipoles) with curves represented by symbols given in the legends indicating measured values of phase function for 3 targets and experimental values.

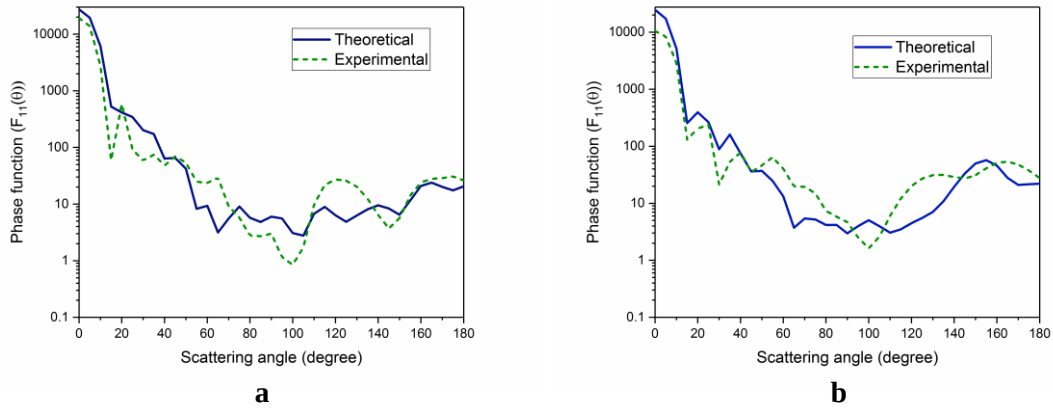

Figure 4.11 (a) Plot of computed results for best possible shape averaged values of phase function (Target2) versus experimental values for 543.5nm incident wavelength. (b)Plot of computed results for best possible shape averaged values of phase function (Target2), versus experimental values for 632.8nm incident wavelength.

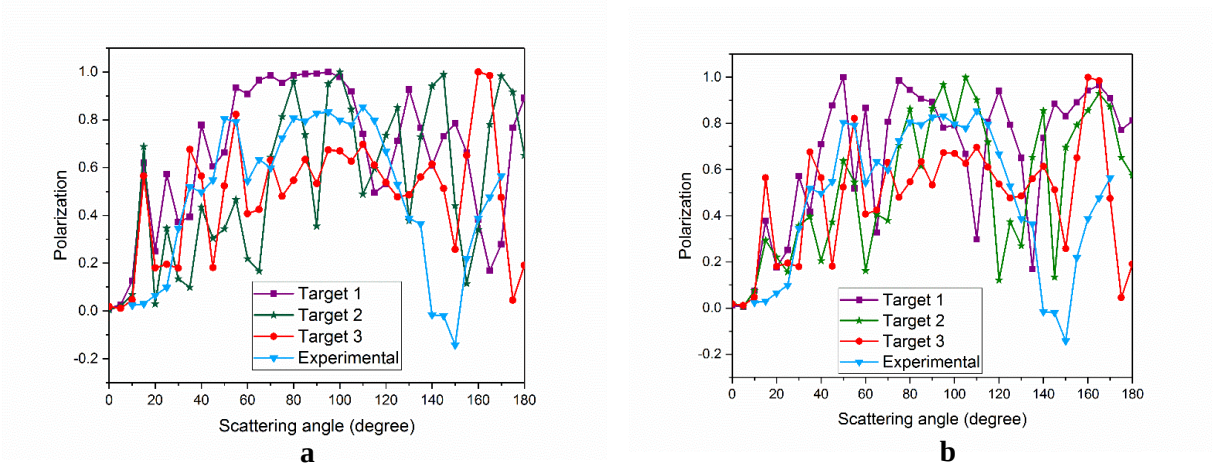

Figure 4.12 (a) Polarization for model shape1 at 543.5nm incident wavelength with curves represented by symbols given in the legends indicating computed values of phase function for 3 targets and experimental values. (b) Polarization for model shape2 at 543.5 nm incident wavelength with curves represented by symbols given in the legends indicating computed values of phase function for 3 targets and experimental values.

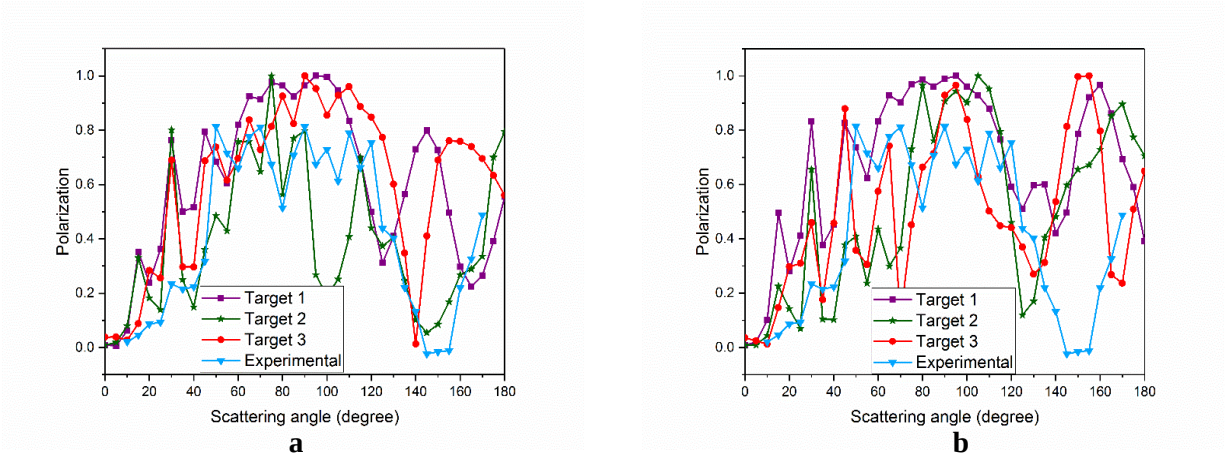

Figure 4.13 (a) Polarization for model shape1 at 632.8 nm incident wavelength (25,465 dipoles) with curves represented by symbols given in the legends indicating measured values of phase function for 3 targets and experimental values. (b) Polarization for model shape1 at 632.8 nm incident wavelength (34,681 dipoles) with curves represented by symbols given in the legends indicating measured values of phase function for 3 targets and experimental values.

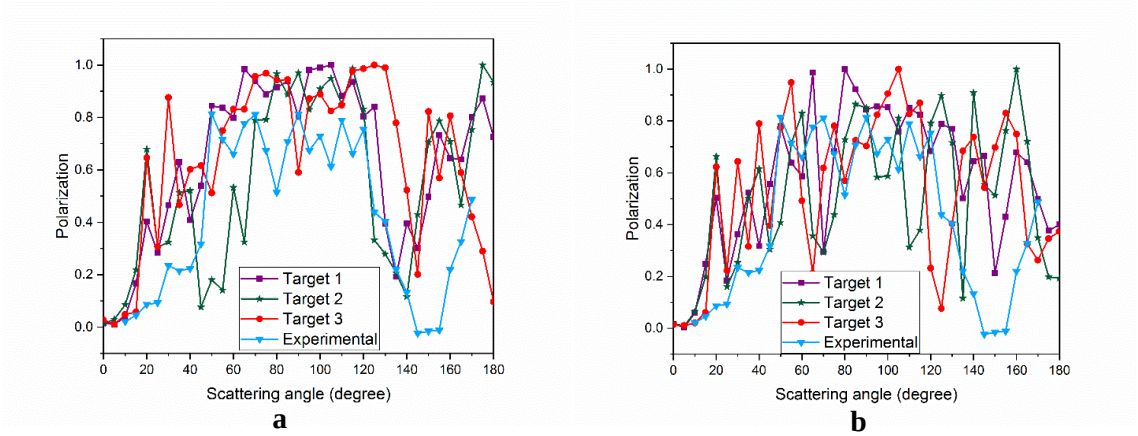

Figure 4.14 (a) Polarization for model shape2 at 632.8 nm incident wavelength (25,465 dipoles) with curves represented by symbols given in the legends indicating measured values of phase function for 3 targets and experimental values. (b) Phase function for model shape2 at 632.8 nm incident wavelength (34,681 dipoles) with curves represented by symbols given in the legends indicating measured values of phase function for 3 targets and experimental values.

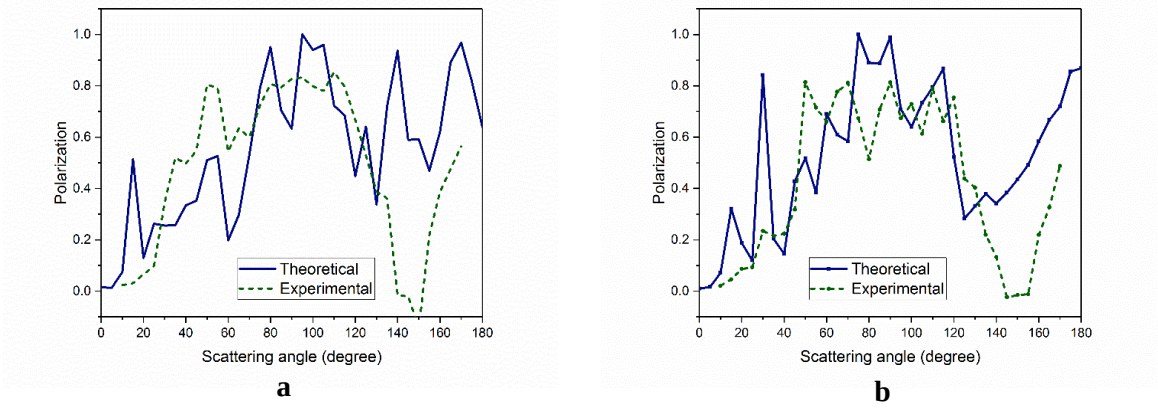

Figure 4.15 (a) Plot of computed results for best possible shape averaged values of polarization (Target2) versus experimental values for 543.5 nm incident wavelength. (b) Plot of computed results for best possible shape averaged values of polarization (Target2), versus experimental values for 632.8 nm incident wavelength.

From the comparative study it is found that software based modeling of irregular 3D geometries and simulations of scattering properties can provide reasonable information about size and shape distributions of realistic samples. It is observed that the shape averaged values

of $F_{11}(\theta)$ for target geometries as single irregular shaped particles with added roughness (Target 2, described in section 4.2) provides the best possible computational fits as compared to the experimental results for both the incident wavelengths used. However slight deviations of the experimental results from the calculated values were observed in case of the polarization. The measured polarization results showed typical negative values of polarization for both the incident laser wavelengths at higher scattering angles which was not found in the DDA calculated values using the present computational model. This might be due to the high irregularities and complex size and shape dispersion of the laboratory graphite samples. Notably, in the present model we have considered a few of the shapes (supposed to consist majority of the samples) and the size distribution we considered is also a standard log normal size distribution closely resembling the sample. Interestingly, in most of the cases, the computations for Target3 of both the shapes, where the model shape was assumed to be composed of spherical monomers of small particles, showed second best agreements with those of experimental values when only size averaging was considered (for phase function). But once shape averaging was performed for Target 3, these agreements were found to be inconsistent and substantial deviation from the experimental results were observed. Thus if the sample under consideration is dispersed only in terms of size, this approach (approach 'c' described in section 4.2) of modeling the target particle may be sufficient to provide good theoretical approximation. But the accuracy of the model is found to be increasing for higher number of dipoles. As in this case the 34,681 dipoles produces better results as compared to the set with 25,465 dipoles. It is desirable to use far larger number of dipoles to represent the target volume but our study is restricted by the availability of computational resources which in turn limits the maximum number of dipoles that could be used in our computation.

Therefore, it can be concluded that modeling of target particles as single irregular shapes accounting for the surface roughness is a better way to explain experimentally observed scattering properties of extremely irregular graphite particle ensembles used in the laboratory simulation.

4.3 Light scattering studies of fayalite dust analogues

Silicates are one of the most studied dust species due to their ubiquity in different astrophysical environments including the solar system, interstellar dust clouds, intergalactic dust clouds, circumstellar dust rings, cometary comae and tails, asteroidal and planetary atmospheres [19-22]. These species are detected in both amorphous and crystalline form with variable iron and magnesium contents which fits well into observed dust spectra [23-26]. Olivine and pyroxene are observed with direct evidences by Infrared Space Observatory (ISO) and the Cosmic Dust Analyzer (CDA) on board the Cassini spacecraft in dust systems [27].

Crystalline olivine is an important component of dust models which includes isomorphous magnesium iron silicates having the general formula $Mg_{2x}Fe_{2-2x}Si0_4$ with $1<x<0$. Fayalite, Fe_2Si0_4 (x=0), is the iron end-member and forsterite, Mg_2Si0_4 (x=l), the magnesium end-member of the olivine group [28]. The iron rich species of olivine (fayalite) is mostly found in interstellar medium and meteorites [29-31]. The magnesium rich olivines and pyroxenes (forsterite, enstatite etc.) are studied extensively to develop dust models [32-35]. But the iron rich silicates, i.e. fayalites, are not abundantly found in earth, which leads to a lack of experimental data for this element to carry out comparative analyses with computations and astrophysical observations despite its importance in dust models. This section provides a simulation study with laboratory synthesized fayalite dust analogues.

4.3.1 Synthesis of fayalite dust samples

Fayalite is a rare element in nature or earth's crust so it is important to synthesize this sample for laboratory characterization in different size distributions as per requirements of experiments [36]. To represent interstellar dust particles these particles sizes must be in the submicron to micrometer range. A sol-gel technique is adopted to synthesize nanocrystalline fayalite (nanofayalite), originally described by De Angelis is adopted [37].

In this method Iron (II) chloride, sodium ethoxide, and tetraethyl orthosilicate (TEOS) were added using a sol-gel process and a precursor gel is produced. This gel was subsequently calcined under reducing conditions to produce crystallize nanofayalite. X-ray diffraction (XRD) analyses indicate that the produced nanofayalite is nearly pure, with minor

amounts of metallic Fe in some batches. The flowchart of sample preparation is shown in Figure 4.16.

At first 375 mL of toluene and 175 mL of methanol were added in a three neck round bottom flask. After that the solvents were refluxed to remove any dissolved oxygen at a temperature of 250° C for about 30 min and then allowed to cool to room temperature. In the next step 8.7 g of iron (II) chloride ($FeCl_2$) followed by 9.3 g of sodium ethoxide (C_2H_5ONa) were during a rigorous stirring process. Sodium ethoxide reacts very rapidly with iron (II) chloride changing the color of the solution from nearly-translucent light to an opaque, grayish-green. This step is followed by the addition of 7.9 g of Tetraethyl orthosilicate (TEOS) while raising the temperature to 150° C. The solution was continuously refluxed for nearly 20–30 min, and after that 10 mL solution of 0.2 M NaOH was slowly dripped with a syringe to hydrolyze the iron (II) ethoxide and TEOS. The solution was then allowed to reflux for another 12 h. After the reaction is over, heating was turned off and the solution was cooled down. In the following step a rotary evaporator was used for solvent removal and drying. The dried powder was the calcined in a tube furnace under flowing N_2 gas for 4 h at a high temperature of 800° C. After calcination, the nanofayalite crystals were rinsed using centrifuge process repeatedly with hot deionized H_2O to remove all the NaCl. Finally after removal of NaCl, the produced fayalite crystals were rinsed with methanol and dried with a rotary evaporator again [37].

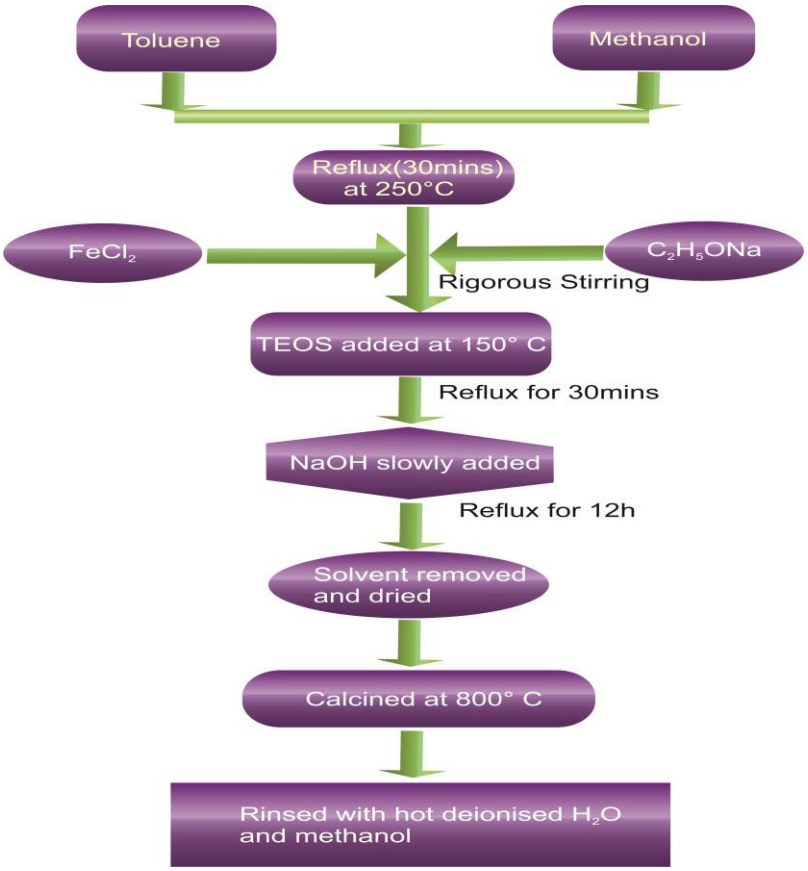

Figure 4.16 Flowchart for sol-gel synthesis of fayalite.

4.3.2 Characterization of fayalite particles

Scanning Electron Microscopy (SEM) and Energy-dispersive X-ray spectroscopy (EDX)

For morphological and particle size distribution studies of the synthesized fayalite samples, SEM was employed. The high resolution SEM images revealed the particles to be of diverse surface topography characterized irregularities in their geometries [Figure 4.17(a) and 4.17(b)]. The images clearly shows particles with considerable surface roughness. As calculated from the images the particle sizes are found to be ranging from 0.3 μm to 4 μm. Some distinct shapes (mostly irregular) are selected and later used for generation of target geometries for the simulation work.

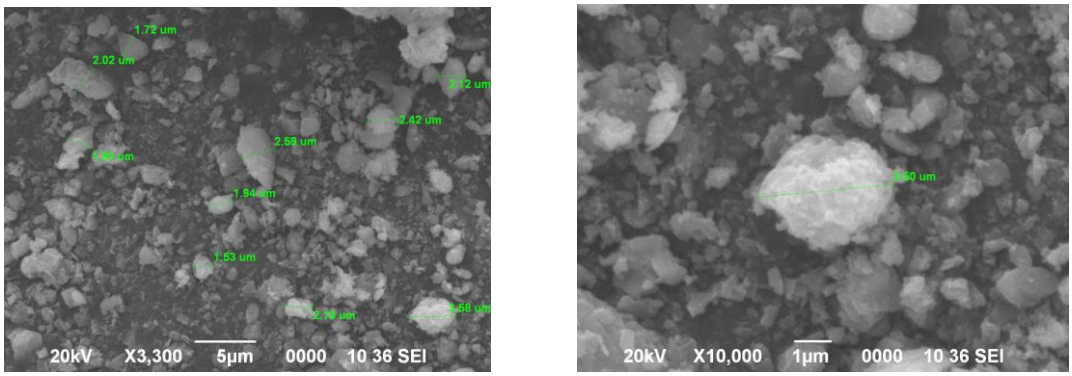

a **a**

Figure 4.17 (a) and (b) HR-SEM images of laboratory synthesized fayalite micro particles.

Again for determination of elemental composition and confirmation, EDX in combination with SEM was performed on the prepared samples and the results are shown in Figure 4.18. The data analysis revealed the '% weight', '% atomic' and characteristic energy-level shells responsible for emission from the elements Fe, Si, and O. These energy spectra is tabulated and shown in Table 4.3. The symbol 'K' in the table signifies that energy peak for the particular element in the EDX spectra corresponds to the X-rays emission from K energy shell. All the known characteristic peaks of Fe, O and Si were observed at their respective energy levels. A peak for Na was observed near 1.1 keV due to the residual Na left out after the application of all the NaCl removal procedures.

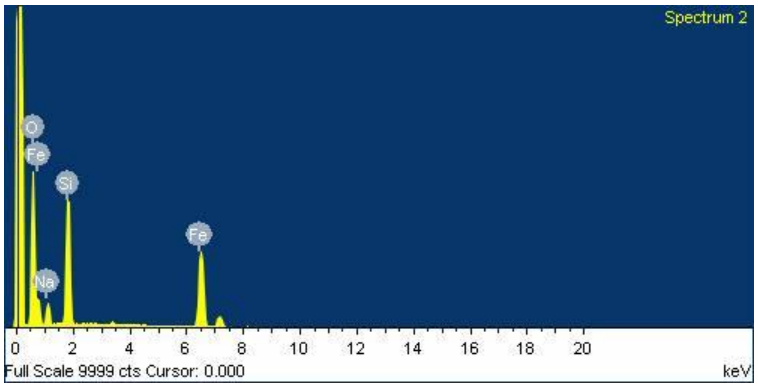

Figure 4.18 EDX spectroscopy analysis of laboratory synthesized fayalite microparticles.

Table 4.3 Composition of the synthesized fayalite particles as determined by EDX analysis

Element	Weight%	Atomic%
O K	49.69	68.49
Na K	7.87	7.55
Si K	18.45	14.49
Fe K	23.98	9.47
Totals	100.00	100.00

4.3.3 X-ray diffraction (XRD) analysis

XRD was employed phase analysis of the particles. The XRD patterns are shown in Figure 4.19. The symbols '+' and '*' represents orthorhombic and cubic crystal structures respectively. The XRD analysis revealed crystalline properties of the characterized samples. The peaks observed at 2θ = 16.92 º, 20.06º, 25.10º, 29.37º, 31.34 º, 33.75 º, 34.22 º , 35.91 º, 41.31 º, 43.67 º , 45.68 º, 49.48 º , 49.74 º, 51.17 º , 51.51 º , 53.82 º, 54.66 º ,57.42 º, 58.05 º , 61.17 º , 62.31 º , 63.73 º, 64.82 º, 65.25 º and 68.04 º correspond to diffractions at the crystal planes (020), (110), (111), (002), (130), (022), (040), (112), (122), (132), (042), (113), (151), (222), (240), (241), (061), (043), (310), (062), (321), (330), (114), (170), and (261) for orthorhombic structures of fayalite in the sample when compared with Joint Committee on Powder Diffraction Standards Database, JCPDS nos- 76-0512 and 70-1861. While the peaks at 2θ = 18.64 º, 30.67 º, 36.14 º, 37.80 º, 43.93 º, 48.11 º, 54.54 º, 58.15 º, 63.88 º, 67.19 º, 68.27 º, correspond to diffraction at the crystal planes (111), (220), (311), (222), (400), (331), (422), (511), (440), (531) and (442) for cubic structure of fayalite when compared with JCPDS no- 83 – 1654. There are several other strong peaks that were unaccounted for in the XRD plots which indicate the presence of a number of other crystal structures. In addition to these some of the peaks corresponds to two or three types of crystal structures of the sample under consideration. Overall the multiple sharp and intense peaks observed in the XRD analysis indicate that the prepared sample is highly polycrystalline, composed of randomly oriented crystals of different structures and sizes.

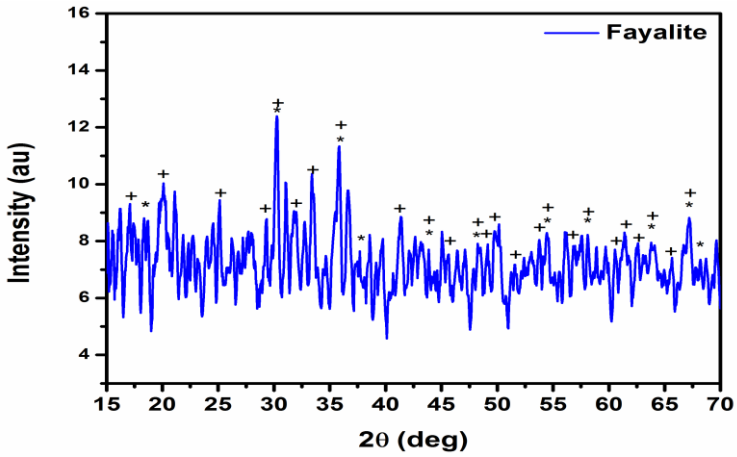

Figure 4.19 XRD spectra of laboratory synthesized fayalite microparticles.

4.3.4 Dust analogue models of fayalite

For the modeling and computational calculation shape models representing realistic fayalite particles (based on the SEM micrographs) were developed [38]. Irregular 3D geometric shapes were generated to represent the majority of particles in the samples. In order to account for the shape dispersions in the prepared samples, two general geometries were selected. A basic sphere in the form of a 3D mesh is selected as the primitive shape to produce the desired arbitrary geometry by modeling. The number of vertices and faces of the primitive basis was increased and after that the individual vertices on the surface or mesh intersections were edited gradually in random directions to create the desired arbitrary shape. To account for the surface roughness, the cloud texture was added followed by a displacement mapping to further deform the target geometry. A number of techniques or approaches to produce the target geometries are adopted and the best possible approach is found out by comparative analyses of the computational data with the experimentally acquired results. Different material densities were considered setting the aspect ratios in between 1 to 3 [38]. The generated final target geometries are shown in the Figure 4.20 and 4.21.

The total number of dipoles was fixed at 10^5 (0.1 million) for both the model target geometries.

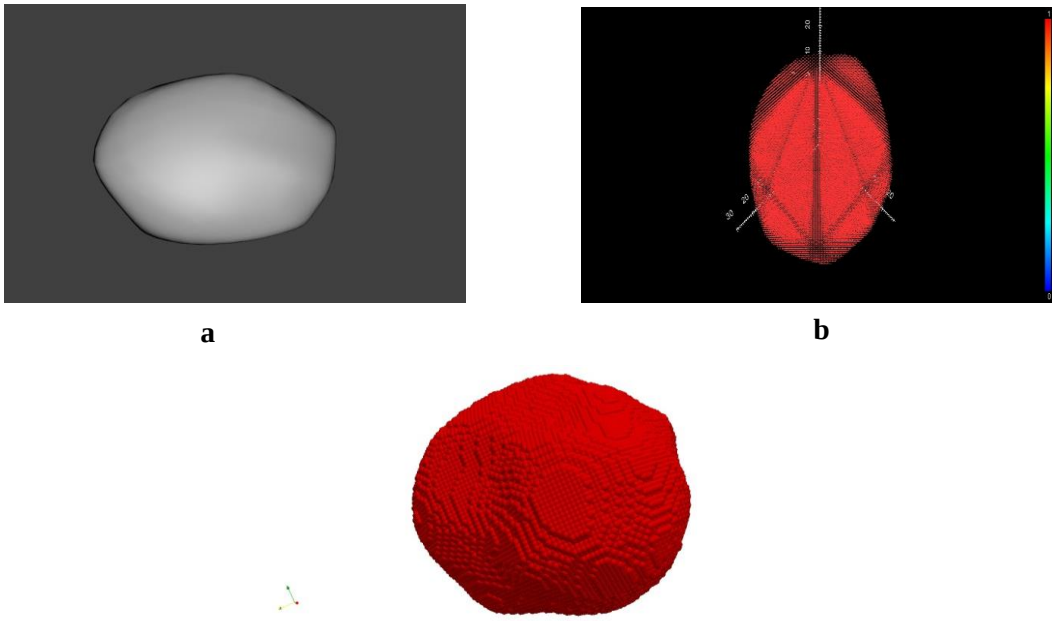

a **b**

c

Figure 4.20 (a) The target geometry 1 generated with Blender3D, (b) 3D rendered images of the model shape after conversion in DDSCAT Convert, (c) Dipole representation of the target particle.

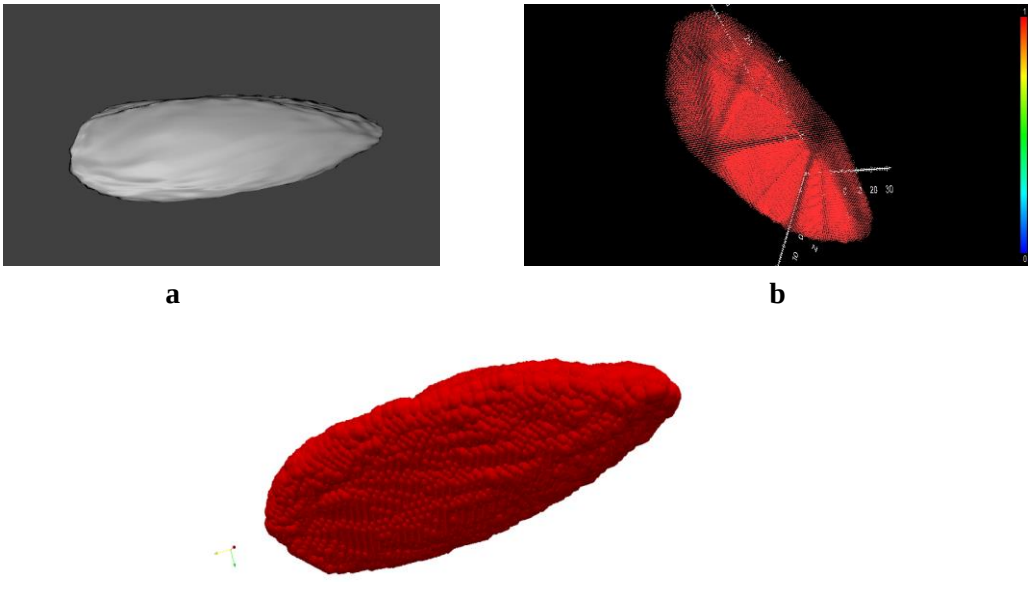

a **b**

c

Figure 4.21 (a) The target geometry 2 generated with Blender3D, (b) 3D rendered images of the model shape after conversion in DDSCAT Convert, (c) Dipole representation of the target particle.

4.3.5 DDA computations and comparative study with experimental results

For carrying out the computations in DDSCAT, the interdipole separation (d) should be fixed within the limit of equation (5) to validate the DDA condition [7],

$$|m|kd \leq 1 \qquad \textbf{4.3}$$

where m is the complex refractive index of the target material, and $k \equiv \frac{2\pi}{\lambda}$ where λ is the wavelength in vacuum. But to satisfy experimental requirements the calculations must be carried on beyond the permissible limit.

As evident from the laboratory synthesized sample the $|m|kd$ value, as specified in the DDA FORTRAN code, was not satisfied for all the cases in this computation. It is possible to cut off the calculation at 1 μm, but in this case the refractive index values especially the imaginary part is crucial provided the shape is fixed [39]. Having fixed the dipole numbers at 10^5 (0.1 million) in our computations, the DDA criterion was satisfied upto maximum particle size of 1.1 microns for incident wavelength of 543.5 nm with $|m|kd = 0.994$, upto 1.3 μm for 594.5 nm with $|m|kd = 0.99867$ and 1.6 μm for 632.8 nm with $|m|kd = 0.9973$. To minimize the effects of errors arising due to the disagreement with the convergence condition, size and shape averaging of the sample were done along with orientational averaging over a number of directions, considering randomness of the errors [39]. The target particle orientation is DDA is defined by using three angles in the target frame namely β, ϕ and θ. The orientational averaging is achieved by running the β and ϕ from 0^0 to 360^0 and θ from 0^0 to 180^0. In this computation the number of directions considered for averaging are 48 [7].

The fayalite samples were nonspherical and highly irregular and distributed over a wide range of shape and size distributions shown in SEM images (Figure 4.17(a) and (b)). The effective radii of the fayalite particles were also estimated using the images. A lognormal size distribution (equation 4.4) was used to fit these samples with a modal radius of 0.75 μm and standard deviation of 1.1. The particle size distribution parameters are given in Table 4.4 and the shape of the distribution curves are shown in Figure 4.22.

Table 4.4 Particle size distribution parameters for fayalite

Size Distribution	**Lognormal(Gaussian)**
Minimum particle radius	0.3 μm
Maximum particle radius	4.0 μm
Modal radius (r_g)	0.75 μm
Standard deviation (σ_g)	1.1

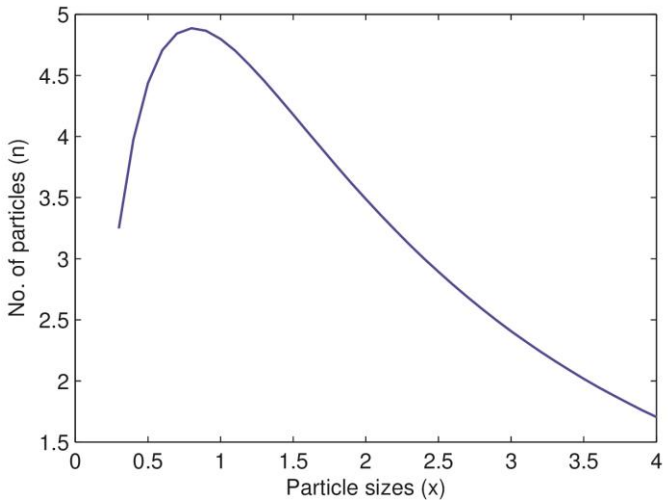

Figure 4.22 Particle size distribution of fayalite.

In order to test the accuracy and efficiency of the size and shape averaged dust particle models the phase function, $F_{11}(\theta)$ and degree of linear polarization $-F_{12}(\theta)/F_{11}(\theta)$, were measured for the samples at 543.5 nm, 594.5 nm and 632.8 nm laser wavelengths and then compared with the computational results.

For calculation of scattering matrix elements, the values of refractive indices for amorphous fayalite were used as tabulated in Table 4.5 [24, 40]. The refractive index values for amorphous fayalite was chosen because of the highly polycrystalline (XRD results in Figure 4.19) nature of the particles and its random orientations in the scattering volume. Besides, it is extremely difficult to measure or find texts providing the refractive index values for the three crystallographic orientation directions of fayalite. Additionally, since the number of dipoles in this computations is very high 10^5 (0.1 million), considering our

computational limitations, the calculations could not go beyond a few thousands of dipoles when an attempt was made to assign each of the dipoles three refractive indices values along the three crystallographic axes. Nevertheless, using the refractive indices for amorphous fayalite gave reasonable values of the two computed scattering parameters as found out by comparing with the experimental results.

The scattering parameters are first computed for both the target geometries considering the size distribution of the samples. The shape averaging is done over the normalized values of the parameters at all three incident wavelengths to find the best fit which can explain the experimentally acquired results. Finally the comparative analyses of the size and shape averaged computed and experimental values of $F_{11}(\theta)$ and $-F_{12}(\theta)/F_{11}(\theta)$ are done for 543.5 nm (Figure 4.23 (a) and 4.23 (b)) 594.5 nm (Figure 4.24 (a) and 4.24 (b)) and 632.8 nm (Figure 4.25 (a) and 4.25 (b)) incident wavelengths are provided.

Table 4.5 Refractive index of fayalite

Wavelength	**Refractive Index (real)** **n**	**Refractive Index (imaginary)** **k**
543.5 nm	1.84452573	0.00087469
594.5 nm	1.8460212	0.00108154
632.8 nm	1.89643342	0.00144143

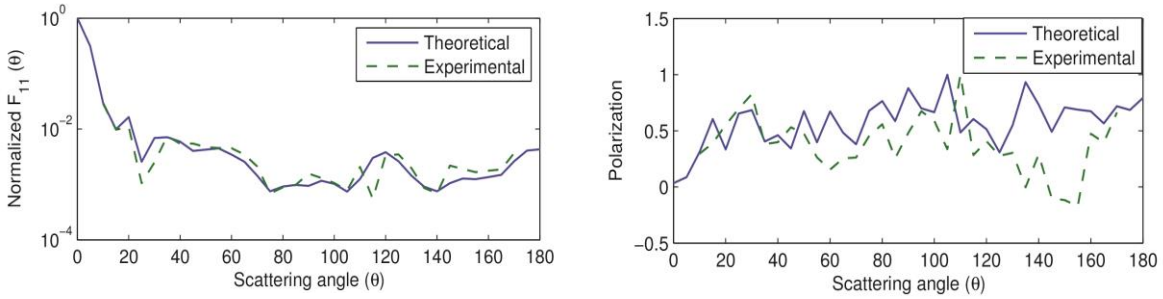

a **b**

Figure 4.23 (a) Size and shape averaged values of Phase function at 543.5 nm incident wavelength with curves represented by legends indicating computed and experimental values. (b) Size and shape averaged values of Polarization at 543.5 nm incident wavelength with curves represented by legends indicating computed and experimental values.

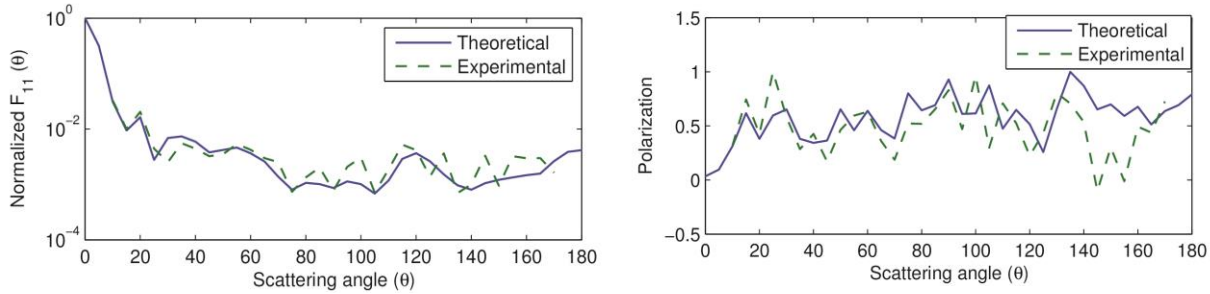

a **b**

Figure 4.24 (a) Size and shape averaged values of Phase function at 594.5 nm incident wavelength with curves represented by legends indicating computed and experimental values. (b) Size and shape averaged values of Polarization at 594.5 nm incident wavelength with curves represented by legends indicating computed and experimental values.

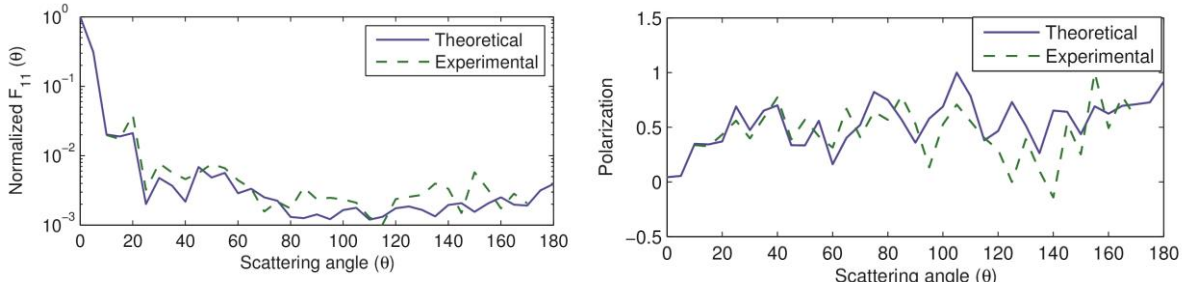

a **b**

Figure 4.25 (a) Size and shape averaged values of Phase function at 632.8 nm incident wavelength with curves represented by legends indicating computed and experimental values. (b) Size and shape averaged values of Polarization at 632.8 nm incident wavelength with curves represented by legends indicating computed and experimental values.

Single scattering albedo and Asymmetry parameter values

The single scattering albedos and asymmetry parameters for the samples are calculated in the DDA computation and found to be similar to characteristic values of fayalite considering the wavelength range used. The calculated values are provided in Table 4.6 at the three wavelengths 543.5 nm, 594.5 nm and 632.8 nm used in this characterization.

The values are calculated as,

$$Single\ scattering albedo\ (a) = \frac{scattering\ \ cross-section}{extinction\ \ cross-section} \quad \textbf{4.4}$$

$$Asymmetry\ \ parameter\ (g) = \langle \cos theta \rangle \quad \textbf{4.5}$$

Where *cos theta* is the cosine of the scattering angle 'Θ'.

Table 4.6 Single scattering albedo and Asymmetry parameter values of fayalite

Wavelengths	Single scattering albedo (a)	Asymmetry parameter (g)
543.5 nm	0.967889532	5.24115e-01
594.5 nm	0.960773064	5.27155e-01
632.8 nm	0.967294834	5.032e-01

4.3.6 Results and Discussions

The software based modeling of irregular 3D geometries and subsequent simulations of scattering properties, proved to be efficient in reproducing the experimental data of fayalite at all the three laser wavelengths 543.5 nm, 594.5 nm and 632.8 nm. A number of shape models (different geometries) were designed with different roughness and porosity by varying surface deformation and number of dipoles respectively. In other words, we used a combination of shapes with different deformation and dipole number to have a rough approximation for the effects of surface roughness and porosities respectively on measured scattering parameters. In order to achieve near perfect models of the real dust particles used in the experiment, targets are generated using different surface and volume modifiers available in the software used. In this particular work, we have selected the best shapes with corresponding deformation and number of dipoles (two targets in this case) which gave a reasonable fit to the experimentally measured data. Finally a near perfect combination of surface roughness, porosity and size distributions representing the target geometries (or scattering particles) was arrived in the computations. And the final model was able to reproduce the light scattering parameters of randomly oriented polycrystalline fayalite samples quite efficiently.

Notwithstanding the capacity of the reported model to provide good agreement of the computational shape averaged values of $F_{11}(\theta)$ and $-F_{12}(\theta)/F_{11}(\theta)$ with the experimentally measured values, discrepancies were observed at the higher scattering angles, especially for the computational polarization curves, which might be due to the experimental inadequacies. Notably, the accurate measurement of polarization requires very sophisticated and expensive instrumentations. On the other hand, in these experiments a typical negative value of polarization at higher scattering angles (or lower phase angles) appears at all the three laser wavelengths employed. These peaks are earlier observed in case of cometary dust [41, 42]. However this negative branch could not be found in any of the computational polarization curves. This indicates the necessity of some extra parameters including other physical or optical properties of the scattering particles so as to explain these negative peaks. Highly accurate computations for both amorphous and polycrystallites to separate their scattering properties and absorption spectra in astrophysical observational data should be performed for better dust models.

4.4 Conclusions

1. This computational and experimental work with two dust analogue samples graphite and fayalite provides a general idea about computational modeling of irregular particle based on real analogue samples.
2. Interstellar dust analogue irregularly shaped amorphous graphite and polycrystalline fayalite samples produces good models for reproducing laboratory simulation results considering the complexities of both computations and measurement techniques involved.
3. Considering the size distributions of atmospheric aerosols, interstellar and cosmic dust with sizes ranging from a few nanometers to more than 100 μm, the present study need to extended for calculating the entire scattering matrix in the visible to infrared wavelength range.

References

1. Westphal, A.J., Stroud, R.M., Bechtel, H.A., Brenker, F.E., Butterworth, A.L., Flynn, G.J., Frank, D.R., Gainsforth, Z., Hillier, J.K., Postberg, F. and Simionovici, A.S., Evidence for interstellar origin of seven dust particles collected by the Stardust spacecraft. *Science*, 345(6198):786-791, 2014.
2. Mishchenko, M.I., Travis, L.D., Kahn, R.A. and West, R.A., Modeling phase functions for dustlike tropospheric aerosols using a shape mixture of randomly oriented polydisperse spheroids. *Journal of Geophysical Research: Atmospheres*, 102(D14):16831-16847, 1997.
3. Brownlee, D.E., Pilachowski, L., Olszewski, E. and Hodge, P.W., January. Analysis of interplanetary dust collections. In *Symposium-International Astronomical Union*, volume 90, pages 333-342, Cambridge University Press, 1980,
4. Vaidya, D.B., Gupta, R. and Snow, T.P., Composite interstellar grains. *Monthly Notices of the Royal Astronomical Society*, 379(2):791-800, 2007.
5. Kissel, J., Glasmachers, A., Grün, E., Henkel, H., Höfner, H., Haerendel, G., Von Hoerner, H., Hornung, K., Jessberger, E.K., Krueger, F.R. and Möhlmann, D., Cometary and interstellar dust analyzer for comet Wild 2. *Journal of Geophysical Research: Planets*, 108(E10), 2003.
6. Savage, B. D., and Sembach, K. R., Interstellar abundances from absorption-line observations with the Hubble Space Telescope. *Annual Review of Astronomy and Astrophysics*, 34(1):279-329, 1996.
7. Draine, B.T. and Flatau, P.J., User guide for the discrete dipole approximation code DDSCAT 7.3, 2013. url: https://arxiv.org/abs/1305.6497.
8. Flatau, P.J. and Draine, B.T., Light scattering by hexagonal columns in the discrete dipole approximation. *Optics express*, 22(18):21834-21846, 2014.
9. Blender. Web reference: https://www.blender.org/. Date accessed: 30th April, 2018.
10. Feser, J. and Sobh, A.N., DDSCAT Convert: A Target Generation Tool, 2013. https://nanohub.org/resources/ddaconvert.

11. Shen, Y., Draine, B.T. and Johnson, E.T., Modeling porous dust grains with ballistic aggregates. II. Light scattering properties. *The Astrophysical Journal*, 696(2):2126, 2009.
12. Draine, B.T. and Li, A., Infrared emission from interstellar dust. IV. The silicate-graphite-PAH model in the post-Spitzer era. *The Astrophysical Journal*, 657(2):810, 2007.
13. Pei, Y.C., Interstellar dust from the Milky Way to the Magellanic Clouds. *The Astrophysical Journal*, 395:130-139, 1992.
14. Draine, B.T. and Lee, H.M., Optical properties of interstellar graphite and silicate grains. *The Astrophysical Journal*, 285:89-108, 1984.
15. Mathis, J.S., Rumpl, W. and Nordsieck, K.H., The size distribution of interstellar grains. *The Astrophysical Journal*, 217:425-433, 1977.
16. Heintzenberg, J., Properties of the log-normal particle size distribution. *Aerosol Science and Technology*, 21(1):46-48, 1994.
17. Gogoi, A., Borthakur, L.J., Choudhury, A., Stanciu, G.A. and Ahmed, G.A., Detector array incorporated optical scattering instrument for nephelometric measurements on small particles. *Measurement Science and Technology*, 20(9):095901, 2009.
18. Ahmed, G.A. and Gogoi, A., Scattering by interstellar graphite dust analog. *Journal of Quantitative Spectroscopy and Radiative Transfer*, 146:106-112, 2014.
19. Kemper, F., Markwick, A.J. and Woods, P.M., The crystalline fraction of interstellar silicates in starburst galaxies. *Monthly Notices of the Royal Astronomical Society*, 413(2):1192-1199, 2011.
20. Van der Plas, G., van den Ancker, M.E., Fedele, D., Acke, B., Dominik, C., Waters, L.B.F.M. and Bouwman, J., The structure of protoplanetary disks surrounding three young intermediate mass stars-I. Resolving the disk rotation in the [OI] 6300 Å line. *Astronomy and Astrophysics*, 485(2):487-495, 2008.
21. Molster, F.J., Waters, L.B.F.M., Tielens, A.G.G.M., Koike, C. and Chihara, H., Crystalline silicate dust around evolved stars. III. A correlations study of crystalline silicate features, *AandA, 3*82(1):241-255, 2002.

22. van Boekel, R., Dullemond, C.P. and Dominik, C., Flaring and self-shadowed disks around Herbig Ae stars: simulations for 10 μm interferometers. *Astronomy and Astrophysics*, 441(2):563-571, 2005.
23. Tsuchiyama, A., Takahashi, T. and Tachibana, S., Evaporation rates of forsterite in the system Mg2SiO4–H2. *Mineralogical Journal*, 20(3):113-126, 1998.
24. Fabian, D., Henning, T., Jäger, C., Mutschke, H., Dorschner, J. and Wehrhan, O., Steps toward interstellar silicate mineralogy-VI. Dependence of crystalline olivine IR spectra on iron content and particle shape. *Astronomy and Astrophysics*, 378(1):228-238, 2001.
25. Aller, M.C., Kulkarni, V.P., York, D.G., Vladilo, G., Welty, D.E. and Som, D., Interstellar silicate dust in the z= 0.89 absorber toward PKS 1830-211: crystalline silicates at high redshift?, *The Astrophysical Journal*, 748(1):19, 2012.
26. Bowey, J.E. and Adamson, A.J.,. A mineralogy of extrasolar silicate dust from 10-μm spectra. *Monthly Notices of the Royal Astronomical Society*, 334(1):94-106, 2002
27. Altobelli, N., Postberg, F., Fiege, K., Trieloff, M., Kimura, H., Sterken, V.J., Hsu, H.W., Hillier, J., Khawaja, N., Moragas-Klostermeyer, G. and Blum, J., Flux and composition of interstellar dust at Saturn from Cassini's Cosmic Dust Analyzer. *Science*, 352(6283):312-318, 2016.
28. Jäger, C., Molster, F.J., Dorschner, J., Henning, T., Mutschke, H. and Waters, L.B.F.M., Steps toward interstellar silicate mineralogy. IV. The crystalline revolution. *Astronomy and Astrophysics*, 339:904-916, 1998.
29. Molster, F.J., Yamamura, I., Waters, L.B.F.M., Tielens, A.G.G.M., de Graauw, T., De Jong, T., De Koter, A., Malfait, K., Van den Ancker, M.E., Van Winckel, H. and Voors, R.H.M., Low-temperature crystallization of silicate dust in circumstellar disks. *Nature*, 401(6753):563, 1999.
30. Meeus, G., Waters, L.B.F.M., Bouwman, J., Van Den Ancker, M.E., Waelkens, C. and Malfait, K., ISO spectroscopy of circumstellar dust in 14 Herbig Ae/Be systems: Towards an understanding of dust processing. *Astronomy and Astrophysics*, 365(3):476-490, 2001.

31. Weisberg, M.K. and Prinz, M., Fayalitic olivine in CV3 chondrite matrix and dark inclusions: A nebular origin. *Meteoritics and Planetary Science*, 33(5):1087-1099, 1998.
32. Rinehart, S.A., Benford, D.J., Cataldo, G., Dwek, E., Henry, R., Kinzer Jr, R.E., Nuth, J., Silverberg, R., Wheeler, C. and Wollack, E., Measuring the optical properties of astrophysical dust analogues: instrumentation and methods. *Applied optics*, 50(21):4115-4123, 2011.
33. Klöck, W., Thomas, K.L., McKay, D.S. and Palme, H., Unusual olivine and pyroxene composition in interplanetary dust and unequilibrated ordinary chondrites. *Nature*, 339(6220):126, 1989.
34. Krätschmer, W. and Huffman, D.R., Infrared extinction of heavy ion irradiated and amorphous olivine, with applications to interstellar dust. *Astrophysics and Space Science*, 61(1):195-203, 1979.
35. Suto, H., Sogawa, H., Tachibana, S., Koike, C., Karoji, H., Tsuchiyama, A., Chihara, H., Mizutani, K., Akedo, J., Ogiso, K. and Fukui, T., Low-temperature single crystal reflection spectra of forsterite. *Monthly Notices of the Royal Astronomical Society*, 370(4):1599-1606, 2006.
36. Hamilton, V.E., Thermal infrared (vibrational) spectroscopy of Mg–Fe olivines: A review and applications to determining the composition of planetary surfaces. *Chemie der Erde-Geochemistry*, 70(1):7-33, 2010.
37. DeAngelis, M.T., Rondinone, A.J., Pawel, M.D., Labotka, T.C. and Anovitz, L.M., Sol-gel synthesis of nanocrystalline fayalite (Fe2SiO4). *American Mineralogist*, 97(4):653-656, 2012.
38. Boruah, M.J., Gogoi, A. and Ahmed, G.A., Laboratory simulation and modeling of size, shape distributed interstellar graphite dust analogues: A comparative study. *Planetary and Space Science*, 125:27-36, 2016.
39. Vilaplana, R., Luna, R. and Guirado, D., The shape influence on the overall single scattering properties of a sample in random orientation. *Journal of Quantitative Spectroscopy and Radiative Transfer*, 112(11):1838-1847, 2011.

40. Database of Optical Constants for Cosmic Dust, url: http://www.astro.uni-jena.de/Laboratory/OCDB/crsilicates.html
41. Hadamcik, E., Renard, J. B., Rietmeijer, F. J. M., Levasseur-Regourd, A. C., Hill, H. G. M., Karner, J. M., and Nuth, J. A. Light scattering by fluffy Mg–Fe–SiO and C mixtures as cometary analogs (PROGRA2 experiment). *Icarus*, 190(2):660-671, 2007
42. Kimura, H., Kolokolova, L., and Mann, I. Optical properties of cometary dust-Constraints from numerical studies on light scattering by aggregate particles. *Astronomy and Astrophysics*, 407(1):L5-L8, 2003.